ACS OMEGA

http://pubs.acs.org/journal/acsodf

Article

High-Voltage Cathode α-Fe_2O_3 Nanoceramics for Rechargeable Sodium-Ion Batteries

Hanqing Dai,[‖] Wenqian Xu,[‖] Zhe Hu, Jing Gu, Yuanyuan Chen, Ruiqian Guo,* Guoqi Zhang,* and Wei Wei*

Cite This: *ACS Omega* 2021, 6, 12615−12622

Read Online

ACCESS | Metrics & More | Article Recommendations

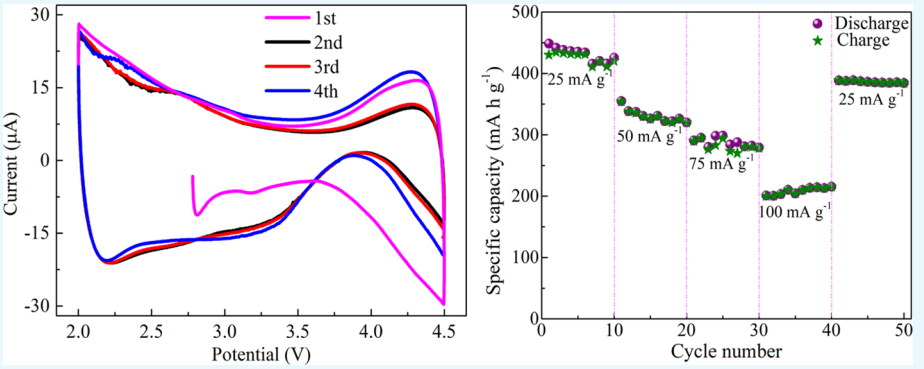

ABSTRACT: Previously, α-Fe_2O_3 nanocrystals are recognized as anode materials owing to their high capacity and multiple properties. Now, this work provides high-voltage α-Fe_2O_3 nanoceramics cathodes fabricated by the solvothermal and calcination processes for sodium-ion batteries (SIBs). Then, their structure and electrical conductivity were investigated by the first-principles calculations. Also, the SIB with the α-Fe_2O_3 nanoceramics cathode exhibits a high initial charge-specific capacity of 692.5 mA h g^{-1} from 2.0 to 4.5 V at a current density of 25 mA g^{-1}. After 800 cycles, the discharge capacity is still 201.8 mA h g^{-1}, well exceeding the one associated with the present-state high-voltage SIB. Furthermore, the effect of the porous structure of the α-Fe_2O_3 nanoceramics on sodium ion transport and cyclability is investigated. This reveals that α-Fe_2O_3 nanoceramics will be a remarkably promising low-cost and pollution-free high-voltage cathode candidate for high-voltage SIBs.

1. INTRODUCTION

Low-cost, pollution-free, high-efficiency, and fail-safe energy storage systems are significant for accomplishing the usually booming requirements of portable electronics, electric vehicles, and intermittent energy conversions, such as wind and solar power. Recently, lithium-ion batteries (LIBs) have bourgeoned into an essential choice due to their long cycling life and high energy density.[1−4] However, the limited availability of lithium resources greatly impedes the large-scale applications of LIBs.[5−7] As a potential supplement, rechargeable sodium-ion batteries (SIBs) have been brought into sharp focus due to the oversupply and sixpenny sodium resources.[5] However, there are two serious issues behind SIBs that affect their applications: one is the ionic size that hinders the sodium-ion diffusion into the crystal structure and the other is the higher potential compared to the lithium.[8−10] These two problems can be solved by identifying suitable low-voltage anode and high-voltage cathode materials. In this context, we have focused on the high-voltage cathodes for SIBs.

For example, the layered oxide P2−$Na_{2/3}Ni_{1/3}Mn_{2/3}O_2$ delivers a low capacity of 89 mA h g^{-1} at 0.05 C after 50 cycles from 2.0 to 4.5 V.[11] Then, $Na_{0.66}Ni_{0.26}Zn_{0.07}Mn_{0.67}O_2$ still delivers a low initial capacity of 132 mA h g^{-1} at 0.1 C with a high average voltage of 3.6 V and capacity retention of 89% after 30 cycles.[12] Recently, the full cell with a layered oxide $Na_{2/3}Ni_{1/6}Mn_{2/3}Cu_{1/9}Mg_{1/18}O_2$ could deliver a low specific capacity of 84.7 mA h g^{-1} in the voltage range of 2.4−4.05 V at 0.2 C after 500 cycles.[13] The NASICON-structured $Na_3V_2(PO_4)_3$ represents one of the most extensively studied positive electrode materials owing to its high ion diffusion rates and long cycle life, and carbon-coated $Na_4Ni_3(PO_4)_2P_2O_7$ electrode delivers a poor discharge capacity of 51 mA h g^{-1}

Received: February 4, 2021
Accepted: April 26, 2021
Published: May 10, 2021

https://doi.org/10.1021/acsomega.1c00640
ACS Omega 2021, 6, 12615−12622

at a 0.1 C rate after 40 cycles.[14] Additionally, a SIB with $Na_3V_2(PO_4)_2F_3$−SWCNT cathode exhibits a specific capacity of 114 mA h g^{-1} at 4.1 V after 100 cycles.[15] Moreover, O3-type cathode $NaNi_{0.4}Mn_{0.25}Ti_{0.3}Co_{0.05}O_2$ maintains 91.4 mA h g^{-1} after 180 cycles at 0.8 C from 2.0 to 4.4 V.[16] However, these cathode materials with poor capacity and specific energy density are unable to meet the needs of the application. Among them, Fe_2O_3 is considered as a promising supplement for SIBs because it is resource-rich, low-cost, and eco-friendly.[28−32] Unfortunately, pure Fe_2O_3 possesses a weak electrical conductivity, making the electrochemical redox reaction difficult. Therefore, pure Fe_2O_3 suffers from relatively poor capacity and low cycling lifetime,[33−37] which limits its commercial value.

To mitigate the poor electrochemical performance of pure Fe_2O_3, one effective method is to develop the composite manufacture of carbon and nano-Fe_2O_3,[38−41] in which carbon materials act as the buffering district, and nano-Fe_2O_3 particles lessen their structure pulverization during the charge−discharge process. Not only does it enhance the electrical conductivity of nano-Fe_2O_3 particles but also it provides excellent flexibility of the large volume change.[26,33,36] Recently, an alternative approach to lessen the size of electrode[27] materials and expand the electrode channels has been recommended to sweep away the aforesaid questions.[42−45] Although the reversible capacities of pure nano-Fe_2O_3 obtained by the above two methods are 100−400 mA h g^{-1}, the pure nano-Fe_2O_3 anode materials still have the phenomenon of low conductivity and high structure pulverization. A previous research implied that the short-range defects of α-Fe_2O_3 ceramics in the sintering process can improve the conductivity and retard the pulverization of structure to guarantee long-term cyclability.[46−49] Therefore, the development of α-Fe_2O_3 ceramics should be a remarkably promising method to ameliorate the electrochemical performance of α-Fe_2O_3.

Herein, α-Fe_2O_3 nanoceramics were successfully fabricated and applied for SIBs. Amazingly, the α-Fe_2O_3 nanoceramics could be used as high-voltage cathode materials for SIBs, and they manifest prominent cyclability and a high initial charge-specific capacity of 692.5 mA h g^{-1} in the voltage range of 2.0−4.5 V at a current density of 25 mA g^{-1}. The discharge capacity is still 201.8 mA h g^{-1} after 800 cycles, that is, a value well exceeding the one associated with the present-state high-voltage SIB. The effect of the α-Fe_2O_3 nanostructures on performances was investigated thoroughly. The electrical conductivity of α-Fe_2O_3 was investigated by the first-principles. The results reveal that appropriate sintering conditions can facilitate centralized micropores in a short time with low energy consumption and form an intimate and substantial contact among α-Fe_2O_3 nanocrystals, which is crucial for protecting the stability of the α-Fe_2O_3 nanoceramics structure in the charge−discharge process with sodium ions embedded and removed in the α-Fe_2O_3 nanoceramics. These results will provide references for the high-voltage SIB application and development in the future.

2. EXPERIMENTAL SECTION

2.1. Synthesis of Materials. α-Fe_2O_3 nanoceramics were successfully fabricated by the solvothermal and calcination processes. Raw materials include iron chloride hexahydrate, dimethyl terephthalate, *N*,*N*-dimethylformamide, ethanol, and deionized water. First, 3 mmol iron chloride hexahydrate and 2.5 mmol dimethyl terephthalate were completely dissolved in 80 mL of *N*,*N*-dimethylformamide solution. Then, the mixture solution was transferred into a 100 mL Teflon autoclave and then heated at 180 °C for 8 h. After the autoclave cooled at room temperature, the red product was washed by ethanol and dried at 80 °C for 24 h. Finally, the dried red powders were calcined at 380 °C for 2 h under nitrogen conditions and then annealed at 380 °C for 1 h in the air to obtain α-Fe_2O_3 nanoceramics.

2.2. Structure and Morphology Characterization. The structure of the prepared materials was characterized by X-ray diffraction (XRD, Bruker D8 polycrystalline) with Cu Kα radiation (V = 30 kV, I = 25 mA, λ = 1.5418 Å) over the 20 to 80° 2θ range. The chemical states of the samples were obtained by X-ray photoelectron spectroscopy (XPS) with the Escalab 250Xi system at pass energy of 150 eV (1 eV/step), using Al Kα as the exciting X-ray source. The spectra were calibrated with respect to the C 1s peak resulting from the adventitious hydrocarbon, which has an energy of 284.8 eV. The samples were investigated by S4800 scanning electron microscopy (SEM) and JEM-2100 transmission electron microscopy (TEM) and high-resolution TEM (HRTEM; JEM-2s100F, JEOL, Japan).

2.3. Calculation Methods. α-Fe_2O_3 is a hexagonal cell, and its space group is $R\bar{3}c$ (167) with experimental lattice parameters a = 5.0356 nm, b = 5.0356 nm, and c = 13.7489 nm. First-principle calculations were provided by the spin-polarized Generalized Gradient Approximation (GGA) using the Perdew−Burke−Ernzerhof exchange−correlation parameterization to density functional theory utilizing the DMol3 and Cambridge Sequential Total Energy Package (CASTEP) program. Using Perdew−Wang (PW91) density functional engenders the exchange correlation energy. The influences of different k-point samplings and plane wave cutoff energies were explored in a series of test calculations. The Brillouin zone integration was approximated using the special k-point sampling scheme of Monkhorst−Pack, and a 3 × 3×3 k-point grid was used for DMol3. The cutoff energy of the plane wave was 571.4 eV for DMol3. For CASTEP program, a 5 × 5×2 k-point grid was used, and the cutoff energy of the plane wave was 489.8 eV. The maximum root-mean-square convergent tolerance of CASTEP program was less than 2.0 × 10^{-6} eV/atom. The geometry optimization was stopped when all relaxation forces of CASTEP program are less than 0.005 eV/nm. For CASTEP program, the maximum displacement error is within 0.002 nm, and the maximum stress was less than 0.1 GPa.

2.4. Electrochemical Measurement. The working electrode for electrochemical properties was prepared by a mixture of α-Fe_2O_3 nanoceramics, polyvinylidene fluoride, and acetylene black (8:1:1, mass ratio). In the presence of trace 1-methyl-2-pyrrolidine, the above materials were mixed to produce a slurry. Then, it was evenly coated on aluminum foil and dried at 80 °C overnight. Finally, a coin cell of CR 2032 was assembled in an argon-filled glovebox with metallic sodium as the counter electrode, a celgard 2400 membrane as the separator, and a mixture of $NaClO_4$ (1.0 mol L^{-1}), ethylene carbonate (EC), and diethyl carbonate (1:1:1, volume ratio) as the electrolyte.

Cyclic voltammogram (CV) of the α-Fe_2O_3 nanoceramics was tested by an electrochemical workstation (CHI660E) in the range of 2.0−4.5 V (vs Na^+/Na) at a scanning rate of 1 mV s^{-1}. The thin-film electrode of α-Fe_2O_3 nanoceramics was used as a working electrode. The counter and reference electrodes

https://doi.org/10.1021/acsomega.1c00640
ACS Omega 2021, 6, 12615−12622

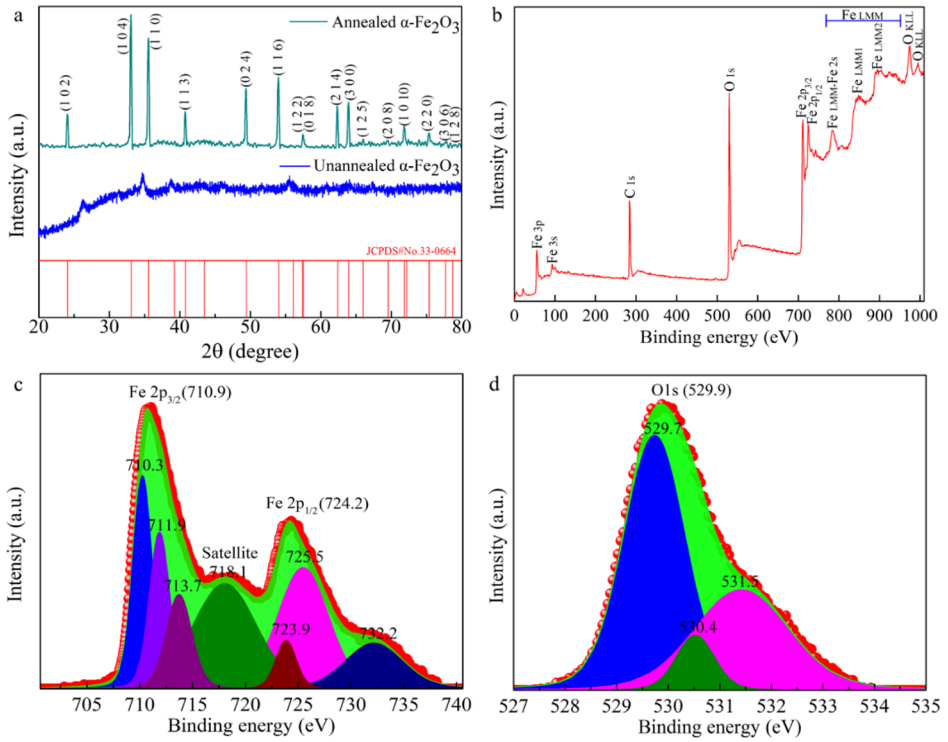

Figure 1. (a) XRD pattern of unannealed α-Fe_2O_3 nanomaterials and annealed α-Fe_2O_3 nanoceramics. (b) Survey XPS spectrum of annealed α-Fe_2O_3 nanoceramics. (c,d) High-resolution XPS spectrum of Fe 2p and O 1s acquired from annealed α-Fe_2O_3 nanoceramics. The black line is the experimental line, and the red line is the simulated line.

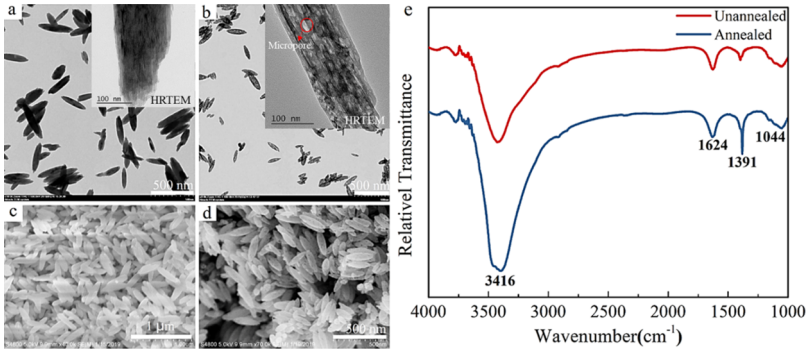

Figure 2. TEM (a) and SEM (c) images of unannealed α-Fe_2O_3 nanomaterials. TEM (b) and SEM (d) images of annealed α-Fe_2O_3 nanoceramics. The illustrations of (a,b) are HRTEM images. (e) FTIR spectra of α-Fe_2O_3 nanomaterials before and after annealing treatment.

were cylindrical stainless-steel ingots. The area of all electrodes is 0.785 cm^2. AC impedance spectroscopy of the coin cell was performed in the frequency range from 0.0001 Hz to 100 kHz. The obtained spectra were fitted using ZView software. Discharge−charge cycling of the coin cell was performed between 2.0 and 4.5 V on CT-2001 LAND battery equipment (Wuhan, China). All the electrochemical measurements were investigated in a dry air atmosphere at room temperature.

3. RESULTS AND DISCUSSION

Figure 1a illustrates the XRD pattern of unannealed α-Fe_2O_3 nanomaterials and annealed α-Fe_2O_3 nanoceramics. It can be seen that there are corresponding diffraction peaks at 27 and 35° in the unannealed material, compared with the well-crystallined FeOOH characteristic peaks.[17] After annealing under certain conditions, nanomaterials became crystalline, giving strong diffraction peaks matching to the characteristic peaks of α-Fe_2O_3 (JCPDS No: 33-0664). No peak intensity of FeOOH is found in all of the fabricated α-Fe_2O_3 nanomaterials compared with the characteristic peaks of FeOOH, which indicate that FeOOH is completely transformed into α-Fe_2O_3 after the heat treatment process. Also, it can be seen that unannealed α-Fe_2O_3 nanomaterials possess poor crystallinity. But all the diffraction peaks of annealed α-Fe_2O_3 nanoceramics can be well assigned to α-Fe_2O_3 (JCPDS card no. 33-0664),[17] indicating better crystallinity. Figure 1b displays a wide XPS survey of α-Fe_2O_3 nanoceramics, which betokens that the samples contained O and Fe elements with sharp photoelectron peaks appearing at the binding energies of 529.9 (O 1s) and 710.9 eV (Fe 2p), respectively. High-resolution XPS spectra of Fe 2p and O 1s were acquired from the α-Fe_2O_3 nanoceramics, as shown in Figure 1c,d. As shown in Figure 1c, the binding energies of the Fe $2p_{3/2}$ and Fe $2p_{1/2}$ peaks of α-Fe_2O_3 are located at 710.9 and 724.2 eV, respectively, with a shakeup satellite peak at 718.1 eV, which are characteristic for the Fe^{3+} species.[18−21] Moreover, the fitted energy difference

https://doi.org/10.1021/acsomega.1c00640
ACS Omega 2021, 6, 12615−12622

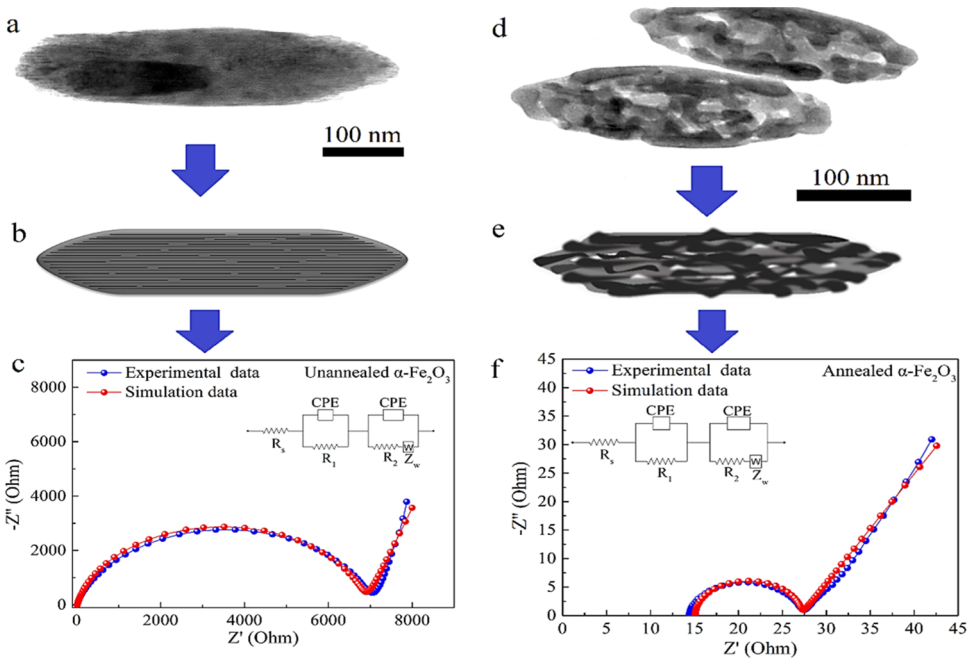

Figure 3. TEM image (a), sketch of structure (b), and Nyquist plots of the unannealed α-Fe_2O_3 nanomaterials (c). TEM image (d), sketch of structure (e), and Nyquist plots of the annealed α-Fe_2O_3 nanoceramics (f). The red lines are the fitting curve by using the equivalent circuits for analysis of the impedance spectra which is shown as the illustrations and consists of the solution resistance of the electrolyte (R_s), a resistor (R_1) paralleled with a constant phase element (CPE), and a CPE paralleled with a resistor (R_2) which is connected with a Warburg element (Z_w) in series. The area of all electrodes is 0.785 cm^2.

between the Fe $2p_{1/2}$ and Fe $2p_{3/2}$ lines is approximately 13.3 eV, which slightly coincides with the reference value ΔE = 13.67 eV for Fe^{3+}.[18−21] As shown in Figure 1d, the peaks around 529.7, 530.4, and 531.5 eV are consistent with the ionic bindings of O. The XPS profile corresponds well to the values of α-Fe_2O_3 reported in the literature.[18−21]

Additionally, morphologies of unannealed α-Fe_2O_3 nanomaterials and annealed α-Fe_2O_3 nanoceramics have been investigated by TEM and SEM, as shown in Figure 2. Some notable differences between the two products can be visible from Figure 2. The structure of unannealed α-Fe_2O_3 nanomaterials composed of crystal nucleus is fine and smooth (Figure 2a). Comparing Figure 2a,b and Figure 2b, it can be found that after annealing, α-Fe_2O_3 could form a microporous structure. From Figure 2b, it can be seen that the pore size is about 10 nm. In order to investigate the influence mechanism of the annealing process on material properties, the FTIR spectra of the samples before and after annealing treatment were carried out with 1000−4000 cm^{-1} (Figure 2e). Compared to the unannealed nanomaterials, the peak intensity of the samples after annealing treatment has a distinct increase at 3416 cm^{-1}. The FTIR peak at 3416 cm^{-1} corresponds to the stretching vibration of −OH. We also find that the peak intensity of the samples at 1391 cm^{-1} after the annealing treatment increases. The polar groups (such as −COOH, −OH, C═O, $-NH_2$, etc.) on or in the α-Fe_2O_3 materials could provide the nucleation site as the template for α-Fe_2O_3 by the coordination of Fe^{3+}. These peak changes (Figure 2e) indicate that the annealing treatment could erode the organic matter in the α-Fe_2O_3 materials, resulting in the formation of the porous structure (Figure 2a,d). Therefore, the prepared precursors were calcined at 380 °C for 2 h under nitrogen conditions and then annealed at 380 °C for 1 h in the air to obtain α-Fe_2O_3 nanoceramics. These pores can promote the insertion and removal of sodium ions. Hence, these structural features make it an outstanding potential electrode material for SIBs.

Conversely, the annealed α-Fe_2O_3 nanoceramics possess some micropores (Figure 3d). Moreover, electrochemical impedance spectroscopy (EIS) measurements were obtained to compare the impedance differences in the unannealed α-Fe_2O_3 nanomaterials and the annealed α-Fe_2O_3 nanoceramics. The Nyquist plots were collected from 0 to 10^5 Hz on the coin-cell batteries after charge−discharge for 10 cycles. As shown in Figure 3c,f, the EIS spectra are fitted by an equivalent circuit and reveal one compressed semicircle followed by a linear part.[22,23] The fitted parameters exhibit that the cells with unannealed α-Fe_2O_3 nanomaterials and annealed α-Fe_2O_3 nanoceramics electrodes possess similar solution resistance of the electrolyte (R_s) of 16.76 and 15.08 Ω, respectively, which represents the good electrical conductivity of the electrolyte. In contrast, the contact impedance (R_1) of the coin cell with the annealed α-Fe_2O_3 nanoceramics is bigger than that of the coin cell with the unannealed α-Fe_2O_3 nanomaterials. Meanwhile, the charge-transfer resistance (R_2) shows significant differences in the two different coin cells. The annealed α-Fe_2O_3 nanoceramics exhibit the much lower value of the charge-transfer resistance (12 Ω) than (6866 Ω) unannealed α-Fe_2O_3 nanomaterials, implying better kinetics for the diffusion of sodium ions in the active material. Thus, the annealed α-Fe_2O_3 nanoceramics cathode shows excellent sodium storage performance. Also, based on the sketches of structure (Figure 3b,e), it can be concluded that the porous structure of the annealed α-Fe_2O_3 nanoceramics facilitates the migration of sodium ions, as reported in the former studies.[22−25]

Ulteriorly, in order to comprehend the electrical conductivity of α-Fe_2O_3, the band structures and density of states of α-Fe_2O_3 crystal were investigated and are shown in Figure

https://doi.org/10.1021/acsomega.1c00640
ACS Omega 2021, 6, 12615−12622

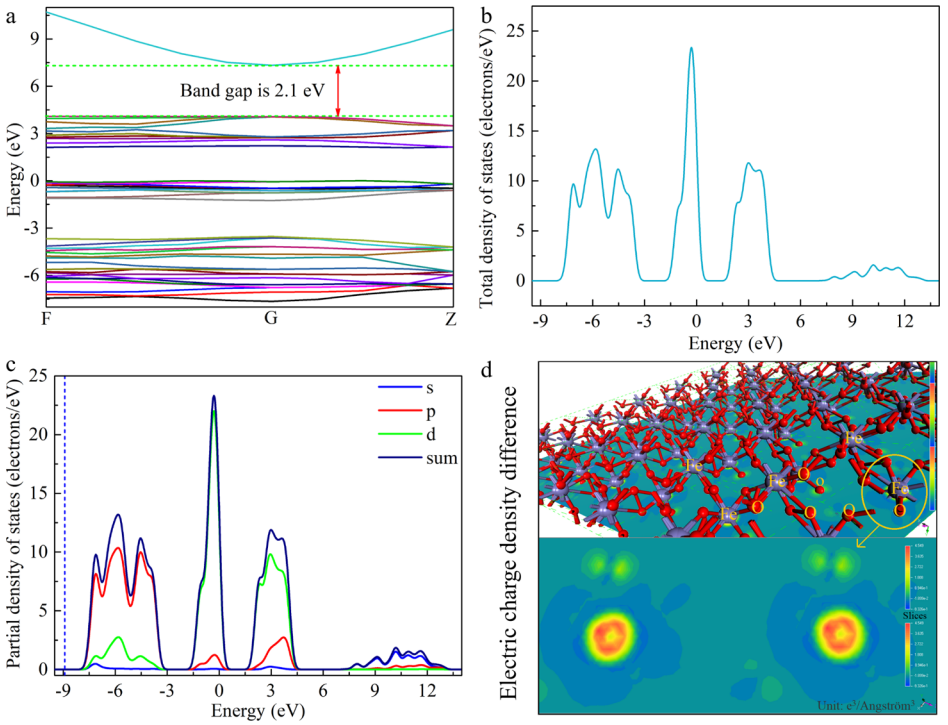

Figure 4. (a) Total band structures of α-Fe_2O_3 crystal. (b) Total density of state of α-Fe_2O_3 crystal. (c) Partial density of states of α-Fe_2O_3 crystal. (d) Electric charge density difference of α-Fe_2O_3 crystal.

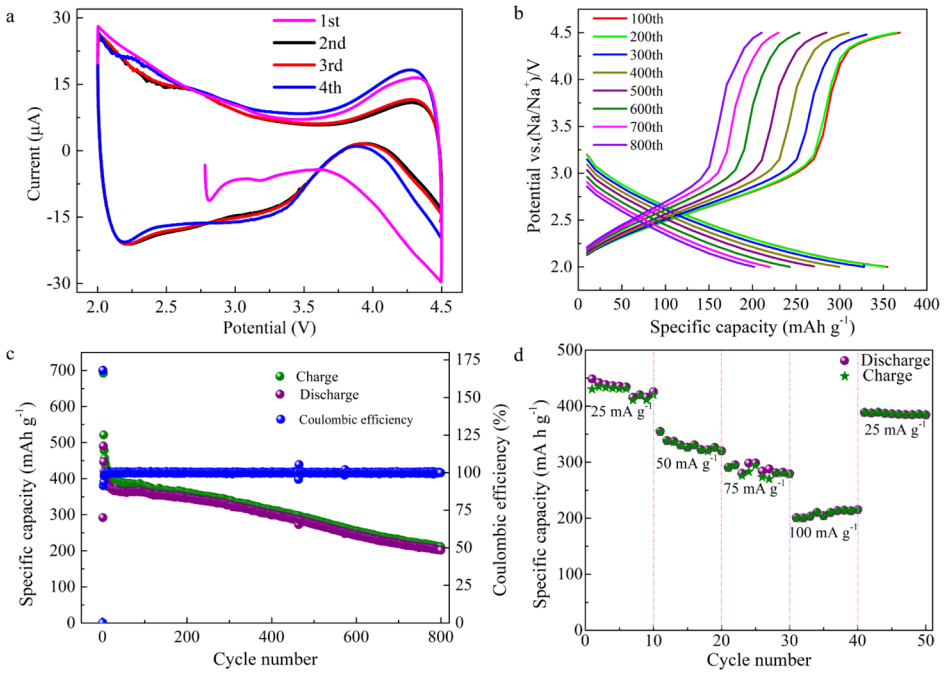

Figure 5. (a) CV curves of α-Fe_2O_3 nanoceramics. (b) Charge−discharge curve of α-Fe_2O_3 nanoceramics between 2.0 and 4.5 V at a current density of 25 mA g^{-1}. (c) Cycle performance of the α-Fe_2O_3 nanoceramics cathode at a current density of 25 mA g^{-1}. (d) Rate performance of α-Fe_2O_3 nanoceramics electrodes.

4a,b, respectively. From Figure 4a, it is clearly seen that the band gap is approximatively 2.1 eV. The calculated Fermi energy is of −8.931 eV. The density of states near the Fermi surface for α-Fe_2O_3 can be evidently observed in Figure 4b,c. The value of density of states near the Fermi surface for α-Fe_2O_3 (~0.0 electrons eV^{-1}) is extremely low. It is generally known that only electrons in the vicinity of the Fermi level can generate the electric current in the external electric field, and the higher band gap means the lower electronic conductivity. Therefore, the α-Fe_2O_3 exhibits low electronic conductivity. The difference in charge density for α-Fe_2O_3 is shown in Figure 4d. It is obvious that the charge density around the iron atom is higher than that around the oxygen atom, and they maintain local charge distribution and structural stability,

https://doi.org/10.1021/acsomega.1c00640
ACS Omega 2021, 6, 12615−12622

which means that the main contribution of the electronic conductivity of the α-Fe_2O_3 cathode material is derived from the iron atoms.

Ultimately, a coin cell of CR 2032 was assembled in an argon-filled glovebox with the α-Fe_2O_3 nanoceramics cathode. Figure 5a illustrates CV curves of α-Fe_2O_3 nanoceramics/Na cell for the first two cycles at a scanning rate of 1 mV s^{-1} in the potential range of 2.0−4.5 V (vs Na^+/Na), which is a quasi-reversible process with a redox reaction (α-Fe_2O_3 + $6Na^+$ + $6e^-$ ↔ 2Fe + $3Na_2O$) between 2.0 and 4.5 V.[28,29] The charge storage of the redox reaction on the surface of the transition-metal oxide anode leads to the pseudocapacitive behavior. Such variation is caused by the unique products in the reduction of Fe_2O_3. Metallic Fe nanoparticles with high conductivity and electrochemically inactive Na_2O are generated after discharging the testing batteries. During the following charging process, the state of Fe and Na_2O will change gradually until the majority of Fe and Na_2O converts to Fe_2O_3 at the end of the oxidation reaction. Thus, during the cycles, the interface of Fe and Na_2O, as well as the conditions and electrochemical activities of the particle surface will change slightly as the reactions progress, influencing the reactions occurring on the surface, which is exactly the pseudocapacitive reaction. These are consistent with the reported results.[50] In the first anodic scan, two major anodic peaks are observed approximately at 2.7 and 4.2 V. In the cathodic sweeps, two major cathodic peaks at 2.6 and 3.3 V are noted. Highly overlapping of four CV traces indicates outstanding cycle ability and repeatability of α-Fe_2O_3 nanoceramics during the charge−discharge process due to the porous structure. These results suggest that α-Fe_2O_3 nanoceramics may be high-voltage cathode materials.

To further validate the above conjecture, Figure 5b records the galvanostatic charge−discharge profiles of α-Fe_2O_3 nanoceramics between 2.0 and 4.5 V at the charging rate of 25 mA g^{-1} (1 C = 1005 mA g^{-1}). It can be seen from analysis that the α-Fe_2O_3 nanoceramics display a large irreversible capacity in the first discharge, which primarily stems from the formation of a solid electrolyte interface (SEI) layer on the surface of α-Fe_2O_3 nanoceramics because of the decomposition of the electrolyte, and sodium ions irreversibly insert into the crystal lattice.[28,29] These results suggest that α-Fe_2O_3 nanoceramics could be high-voltage cathode materials. The cycle performance of the α-Fe_2O_3 nanoceramics cathode at the current density of 25 mA g^{-1} is given in Figure 5c. It is obvious to notice that the high initial charge-specific capacity is 692.5 mA h g^{-1} between 2.0 and 4.5 V at a current density of 25 mA g^{-1}.[17−21,28,29] Since the charge storage of the redox reaction on the surface of the transition-metal oxide anode leads to the pseudocapacitive behavior, which also leads to a sharp drop in the charge-specific capacity. During the following charging process, the state of Fe and Na_2O will change gradually until the majority of Fe and Na_2O converts to Fe_2O_3 at the end of the oxidation reaction. Thus, during the cycles, the interface of Fe and Na_2O, as well as the conditions and electrochemical activities of the particle surface will change slightly as the reactions progress, influencing the reactions occurring on the surface, which is consistent with Figure 5a. After 800 cycles, the discharge capacity is still 201.8 mA h g^{-1}, that is, a value well exceeding the one associated with the present-state high-voltage SIB, as shown in Figure 6.[11−16] Except for a few initial cycles, the Coulombic efficiency is almost 100%, which indicates that the α-Fe_2O_3 nanoceramics have good reversibility. These results demonstrate that sodium ions can be easily embedded and removed from electrode materials, and the redox reaction (α-Fe_2O_3 + $6Na^+$ + $6e^-$ ↔ 2Fe + $3Na_2O$) is a quasi-reversible process. The cyclability is better than that of previous reported high-voltage SIBs, as shown in Figure 6.[11−16] These indicate that the α-Fe_2O_3 nanoceramics have a promising application for high-voltage SIBs as high-voltage cathode materials.

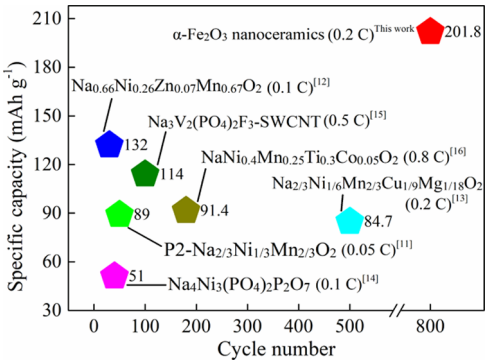

Figure 6. Cycle performance of α-Fe_2O_3 nanoceramics and the reported cathodes applied for the high-voltage SIB between 2.0 and 4.5 V from 2013 to 2020. Photograph courtesy of Hanqing Dai. Copyright 2021.

Simultaneously, the rate performance of the α-Fe_2O_3 nanoceramics cathode was investigated and are illustrated in Figure 5d. The α-Fe_2O_3 nanoceramics cathode demonstrates excellent rate performance and delivers reversible capacities of 420.4, 330.6, 295.3, 213.5, and 386.3 mA h g^{-1} at current densities of 25, 50, 75, 100, and 25 mA g^{-1}, respectively. The results disclose that the α-Fe_2O_3 nanoceramics display an outstanding rate capability and structure stability even at a very high current density. The enhanced electrochemical performance of α-Fe_2O_3 nanoceramics can be attributed to the effect of its porous structure, which closely resembles those reported for SIBs.[28,29] Mostly, the conductive porous structure of the α-Fe_2O_3 nanoceramics can ensure effective and consecutive sodium ion transport and adapt quickly to the volume expansion to avoid the α-Fe_2O_3 nanoceramics being pulverized during the charge−discharge process.[28,29] Additionally, the supply of large surface area of the α-Fe_2O_3 nanoceramics as an ample cathode−electrolyte interface can absorb sodium ions to promote the rapid charge-transfer reaction. The results will provide the references for high-voltage SIB applications and development in the future.

4. CONCLUSIONS

In summary, α-Fe_2O_3 nanoceramics were successfully prepared by the solvothermal and calcination processes, and the practical information about the structure and electrical conductivity could be provided by the first-principles calculations. The electrochemical characteristics were investigated for the application of high-voltage cathodes in SIBs. The SIB with the α-Fe_2O_3 nanoceramics cathode shows a superior initial charge-specific capacity of 692.5 mA h g^{-1} between 2.0 and 4.5 V and a reversible discharge capacity of 201.8 mA h g^{-1} at a current density of 25 mA g^{-1} after 800 cycles. These properties of α-Fe_2O_3 nanoceramics ensure that it will be a promising high-voltage cathode candidate for SIBs.

https://doi.org/10.1021/acsomega.1c00640
ACS Omega 2021, 6, 12615−12622

AUTHOR INFORMATION

Corresponding Authors

Ruiqian Guo − *Institute of Future Lighting, Academy for Engineering and Technology, Institute for Electric Light Sources, Fudan University, Shanghai 200433, China;* orcid.org/0000-0002-0498-0363; Email: rqguo@fudan.edu.cn

Guoqi Zhang − *Department of Microelectronics, Delft University of Technology, Delft 2628 CD, Netherlands*; Email: weiwei@njupt.edu.cn

Wei Wei − *College of Electronic and Optical Engineering & College of Microelectronics, Nanjing University of Posts and Telecommunications, Nanjing 210023, China*; Email: G.Q.Zhang@tudelft.nl

Authors

Hanqing Dai − *Institute of Future Lighting, Academy for Engineering and Technology, Institute for Electric Light Sources, Fudan University, Shanghai 200433, China;* orcid.org/0000-0001-5383-8702

Wenqian Xu − *College of Electronic and Optical Engineering & College of Microelectronics, Nanjing University of Posts and Telecommunications, Nanjing 210023, China*

Zhe Hu − *Institute of Future Lighting, Academy for Engineering and Technology, Institute for Electric Light Sources, Fudan University, Shanghai 200433, China*

Jing Gu − *College of Electronic and Optical Engineering & College of Microelectronics, Nanjing University of Posts and Telecommunications, Nanjing 210023, China*

Yuanyuan Chen − *Institute of Future Lighting, Academy for Engineering and Technology, Institute for Electric Light Sources, Fudan University, Shanghai 200433, China*

Complete contact information is available at: https://pubs.acs.org/10.1021/acsomega.1c00640

Author Contributions

‖H.D. and W.X. authors contributed equally to this work.

Notes

The authors declare no competing financial interest.

ACKNOWLEDGMENTS

Financial support from the National Natural Science Foundation of China (nos. 62075100, 62074044, 61904036, and 61675049), Zhongshan-Fudan Joint Innovation Center and Jihua Laboratory Projects of Guangdong Province (X190111UZ190), and the outstanding doctoral research promotion program of Fudan University (SSH6281011/003) is gratefully acknowledged.

REFERENCES

(1) Lin, Z.; Xia, Q.; Wang, W.; Li, W.; Chou, S. Recent research progresses in ether- and ester-based electrolytes for sodium-ion batteries. *Infomatics* **2019**, *1*, 376−389.

(2) Ma, J.; Li, Y.; Grundish, N. S.; Goodenough, J. B.; Chen, Y.; Guo, L.; Peng, Z.; Qi, X.; Yang, F.; Qie, L.; Wang, C.-A.; Huang, B.; Huang, Z.; Chen, L.; Su, D.; Wang, G.; Peng, X.; Chen, Z.; Yang, J.; He, S.; Zhang, X.; Yu, H.; Fu, C.; Jiang, M.; Deng, W.; Sun, C.-F.; Pan, Q.; Tang, Y.; Li, X.; Ji, X.; Wan, F.; Niu, Z.; Lian, F.; Wang, C.; Wallace, G. G.; Fan, M.; Meng, Q.; Xin, S.; Guo, Y.-G.; Wan, L.-J. The 2020 battery technology roadmap. *J. Phys. D: Appl. Phys.* **2021**, *54*, 183001.

(3) Ding, H.; Zhou, J.; Rao, A. M.; Lu, B. Cell-like-carbon-microspheres for robust potassium anode. *Natl. Sci. Rev.* **2021**, *8*, nwaa276.

(4) Shi, X.; Xu, Z.; Han, C.; Shi, R.; Wu, X.; Lu, B.; Liang, S. Highly dispersed cobalt nanoparticles embedded in nitrogen-doped graphitized carbon for fast and durable potassium storage. *Nano-Micro Lett.* **2021**, *13*, 21.

(5) Dai, H.; Xu, W.; Chen, Y.; Li, M.; Chen, Z.; Yang, B.; Mei, S.; Zhang, W.; Xie, F.; Wei, W.; Guo, R.; Zhang, G. Narrow band-gap cathode $Fe_3(PO_4)_2$ for sodium-ion battery with enhanced sodium storage. *Colloids Surf., A* **2020**, *591*, 124561.

(6) Li, Y.; Lu, Y.; Zhao, C.; Hu, Y.-S.; Titirici, M.-M.; Li, H.; Huang, X.; Chen, L. Recent advances of electrode materials for low-cost sodium-ion batteries towards practical application for grid energy storage. *Energy Storage Mater.* **2017**, *7*, 130−151.

(7) Dai, H.; Chen, Y.; Xu, W.; Hu, Z.; Gu, J.; Wei, X.; Xie, F.; Zhang, W.; Wei, W.; Guo, R.; Zhang, G. A review of modification methods of solid electrolytes for all-solid-state sodium-ion batteries. *Energy Technol.* **2021**, *9*, 2000682.

(8) Sun, J.; Lee, H.-W.; Pasta, M.; Yuan, H.; Zheng, G.; Sun, Y.; Li, Y.; Cui, Y. A phosphorene-graphene hybrid material as a high-capacity anode for sodium-ion batteries. *Nat. Nanotechnol.* **2015**, *10*, 980−985.

(9) Dai, H.; Xu, W.; Yu, K.; Wei, W. Concise synthesis of $NaTi_2(PO_4)_3$ nanocrystals with size and morphology control. *Chin. Chem. Lett.* **2019**, *30*, 517−520.

(10) Dai, H.; Xu, W.; Hu, Z.; Chen, Y.; Wei, X.; Yang, B.; Wei, W. Effective approaches of improving the performance of chalcogenide solid electrolytes for all-solid-state sodium-ion batteries. *Front. Energy Res.* **2020**, *8*, 1−7.

(11) Lee, D. H.; Xu, J.; Meng, Y. S. An advanced cathode for Na-ion batteries with high rate and excellent structural stability[J]. *Phys. Chem. Chem. Phys.* **2013**, *15*, 3304−3312.

(12) Wu, X.; Guo, J.; Wang, D.; et al. P2-type $Na_{0.66}Ni_{0.33-x}Zn_xMn_{0.67}O_2$ as new high-voltage cathode materials for sodium-ion batteries. *J. Power Sources* **2015**, *281*, 18−26.

(13) Xiao, Y.; Zhu, Y. F.; Yao, H. R.; et al. A stable layered oxide cathode material for high-performance sodium-ion battery. *Adv. Energy Mater.* **2019**, *9*, 1803978.

(14) Petla, R. K.; Amin, R.; Belharouak, I.; et al. Electrochemical investigations of high voltage $Na_4Ni_3(PO_4)_2P_2O_7$ cathode for sodium ion batteries[C]//Meeting Abstracts. *J. Electrochem. Soc.* **2019**, *2*, 244.

(15) Liu, S.; Wang, L.; Liu, J.; Zhou, M.; Nian, Q.; Feng, Y.; Tao, Z.; Shao, L. $Na_3V_2(PO_4)_2F_3$−SWCNT: a high voltage cathode for non-aqueous and aqueous sodium-ion batteries. *J. Mater. Chem. A* **2019**, *7*, 248−256.

(16) Zhou, C.; Yang, L.; Zhou, C.; et al. Co-substitution enhances the rate capability and stabilizes the cyclic performance of O3-type cathode $NaNi_{0.45-x}Mn_{0.25}Ti_{0.3}Co_xO_2$ for sodium-ion storage at high voltage. *ACS Appl. Mater. Interfaces* **2019**, *11*, 7906−7913.

(17) Zhang, H.; Li, L.; Liu, C.; Wang, W.; Liang, P.; Mitsuzak, N.; Chen, Z. Carbon coated α-Fe_2O_3 photoanode synthesized by a facile anodic electrodeposition for highly efficient water oxidation. *Electron. Mater. Lett.* **2018**, *14*, 348−356.

(18) Fu, Y. Y.; Wang, R. M.; Xu, J.; Chen, J.; Yan, Y.; Narlikar, A. V.; Zhang, H. Synthesis of large arrays of aligned α-Fe_2O_3 nanowires. *Chem. Phys. Lett.* **2003**, *379*, 373−379.

(19) Hsu, L.-C.; Li, Y.-Y.; Lo, C.-G.; Huang, C.-W.; Chern, G. Thermal growth and magnetic characterization of α-Fe_2O_3 nanowires. *J. Phys. D: Appl. Phys.* **2008**, *41*, 185003.

(20) Zhang, Z.; Hossain, M. F.; Takahashi, T. Self-assembled hematite (α-Fe_2O_3) nanotube arrays for photoelectrocatalytic degradation of azo dye under simulated solar light irradiation. *Appl. Catal., B* **2010**, *95*, 423−429.

(21) Liu, S.-Y.; Xie, J.; Pan, Q.; Wu, C.-Y.; Cao, G.-S.; Zhu, T.-J.; Zhao, X.-B. Graphene anchored with nanocrystal Fe_2O_3 with improved electrochemical Li-storage properties. *Int. J. Electrochem. Sci.* **2012**, *7*, 354−362.

(22) Pan, H.; Lu, X.; Yu, X.; Hu, Y.-S.; Li, H.; Yang, X.-Q.; Chen, L. Sodium storage and transport properties in layered $Na_2Ti_3O_7$ for room-temperature sodium-ion batteries. *Adv. Mater.* **2013**, *3*, 1186−1194.

(23) Wiedenmann, D.; Keller, L.; Holzer, L.; Stojadinović, J.; Münch, B.; Suarez, L.; Fumey, B.; Hagendorfer, H.; Brönnimann, R.; Modregger, P.; Gorbar, M.; Vogt, U. F.; Züttel, A.; Mantia, F. L.; Wepf, R.; Grobéty, B. Three-dimensional pore structure and ion conductivity of porous ceramic diaphragms. *AIChE J.* **2013**, *59*, 1446−1457.
(24) Li, Y.; Wang, Z.; Cao, Y.; Du, F.; Chen, C.; Cui, Z.; Guo, X. W-doped $Li_7La_3Zr_2O_{12}$ ceramic electrolytes for solid state Li-ion batteries. *Electrochim. Acta* **2015**, *180*, 37−42.
(25) Fan, X.; Liu, J.; Song, Z.; Han, X.; Deng, Y.; Zhong, C.; Hu, W. Porous nanocomposite gel polymer electrolyte with high ionic conductivity and superior electrolyte retention capability for long-cycle-life flexible zinc-air batteries. *Nano Energy* **2019**, *56*, 454−462.
(26) Bhide, A.; Hariharan, K. Sodium ion transport in NaPO3-Na2SO4 glasses. *Mater. Chem. Phys.* **2007**, *105*, 213−221.
(27) Yang, S.; Zhang, T.; Tao, Z.; Chen, J. First-principles study on metal-doped $LiNi_{0.5}Mn_{1.5}O_4$ as a cathode material for rechargeable Li-ion batteries. *Acta Chim. Sin.* **2013**, *71*, 1029−1034.
(28) Liu, X.; Chen, T.; Chu, H.; Niu, L.; Sun, Z.; Pan, L.; Sun, C. Q. Fe_2O_3-reduced graphene oxide composites synthesized via microwave-assisted method for sodium ion batteries. *Electrochim. Acta* **2015**, *166*, 12−16.
(29) Zhang, Z.-J.; Wang, Y.-X.; Chou, S.-L.; Li, H.-J.; Liu, H.-K.; Wang, J.-Z. Rapid synthesis of α-Fe_2O_3/rGO nanocomposites by microwave autoclave as superior anodes for sodium-ion batteries. *J. Power Sources* **2015**, *280*, 107−113.
(30) Zhang, S.; Zhang, P.; Xie, A.; Li, S.; Huang, F.; Shen, Y. A novel 2D porous print fabric-like α-Fe_2O_3 sheet with high performance as the anode material for lithium-ion battery. *Electrochim. Acta* **2016**, *212*, 912−920.
(31) Wang, M.; Huang, Y.; Wang, K.; Zhu, Y.; Zhang, N.; Zhang, H.; Li, S.; Feng, Z. PVD synthesis of binder-free silicon and carbon coated 3D α-Fe_2O_3 nanorods hybrid films as high-capacity and long-life anode for flexible lithium-ion batteries. *Energy* **2018**, *164*, 1021−1029.
(32) Shi, L.; Li, Y.; Zeng, F.; Ran, S.; Dong, C.; Leu, S.-Y.; Boles, S. T.; Lam, K. H. In situ growth of amorphous Fe_2O_3 on 3D interconnected nitrogen-doped carbon nanofibers as high-performance anode materials for sodium-ion batteries. *Chem. Eng. J.* **2019**, *356*, 107−116.
(33) Liu, Z.; Tay, S. W. Direct growth Fe_2O_3 nanorods on carbon fibers as anode materials for lithium ion batteries. *Mater. Lett.* **2012**, *72*, 74−77.
(34) Han, F.; Li, D.; Li, W.-C.; Lei, C.; Sun, Q.; Lu, A.-H. Nanoengineered polypyrrole-coated Fe_2O_3@C multifunctional composites with an improved cycle stability as lithium-ion anodes. *Adv. Funct. Mater.* **2013**, *23*, 1692−1700.
(35) Jeong, J.-M.; Choi, B. G.; Lee, S. C.; Lee, K. G.; Chang, S.-J.; Han, Y.-K.; Lee, Y. B.; Lee, H. U.; Kwon, S.; Lee, G.; Lee, C.-S.; Huh, Y. S. Hierarchical hollow spheres of Fe_2O_3@polyaniline for lithium ion battery anodes. *Adv. Mater.* **2013**, *25*, 6250−6255.
(36) Wu, M.; Chen, J.; Wang, C.; Wang, F.; Yi, B.; Su, W.; Wei, Z.; Liu, S. Facile synthesis of Fe_2O_3 nanobelts/CNTs composites as high-performance anode for lithium-ion battery. *Electrochim. Acta* **2014**, *132*, 533−537.
(37) Li, D.; Zhou, J.; Chen, X.; Song, H. Amorphous Fe_2O_3/graphene composite nanosheets with enhanced electrochemical performance for sodium-ion battery. *ACS Appl. Mater. Interfaces* **2016**, *8*, 30899−30907.
(38) Jian, Z.; Zhao, B.; Liu, P.; Li, F.; Zheng, M.; Chen, M.; Shi, Y.; Zhou, H. Fe_2O_3 nanocrystals anchored onto graphene nanosheets as the anode material for low-cost sodium-ion batteries. *Chem. Commun.* **2014**, *50*, 1215−1217.
(39) Cho, J. S.; Hong, Y. J.; Kang, Y. C. Design and synthesis of bubble-nanorod-structured Fe_2O_3-carbon nanofibers as advanced anode material for Li-ion batteries. *ACS Nano* **2015**, *9*, 4026−4035.
(40) Li, H.; Xu, L.; Sitinamaluwa, H.; Wasalathilake, K.; Yan, C. Coating Fe_2O_3 with graphene oxide for high-performance sodium-ion battery anode. *Compos. Commun.* **2016**, *1*, 48−53.
(41) Li, T.; Qin, A.; Yang, L.; Chen, J.; Wang, Q.; Zhang, D.; Yang, H. interfaces, In situ grown Fe_2O_3 single crystallites on reduced graphene oxide nanosheets as high performance conversion anode for sodium-ion batteries. *ACS Appl. Mater. Interfaces* **2017**, *9*, 19900−19907.
(42) Koo, B.; Chattopadhyay, S.; Shibata, T.; Prakapenka, V. B.; Johnson, C. S.; Rajh, T.; Shevchenko, E. V. Intercalation of sodium ions into hollow iron oxide nanoparticles. *Chem. Mater.* **2013**, *25*, 245−252.
(43) Qu, J.; Yin, Y.-X.; Wang, Y.-Q.; Yan, Y.; Guo, Y.-G.; Song, W.-G. Layer structured α-Fe_2O_3 nanodisk/reduced graphene oxide composites as high-performance anode materials for lithium-ion batteries. *ACS Appl. Mater. Interfaces* **2013**, *5*, 3932−3936.
(44) Valvo, M.; Lindgren, F.; Lafont, U.; Björefors, F.; Edström, K. Towards more sustainable negative electrodes in Na-ion batteries via nanostructured iron oxide. *J. Power Sources* **2014**, *245*, 967−978.
(45) Wang, S.; Wei, W.; Pan, Z.; Jiao, S. Hollow α-Fe_2O_3 Nanospheres synthesized using a carbon template as novel anode materials for Na-ion batteries. *ChemElectroChem* **2015**, *1*, 1636−1639.
(46) Santilli, C. V.; Bonnet, J. P.; Dordor, P.; Onillon, M.; Hagenmuller, P. Influence of structural defects on the electrical properties of α-Fe_2O_3 ceramics. *Ceram. Int.* **1990**, *16*, 25−32.
(47) Santilli, C. V.; Bonnet, J. P.; Dordor, P.; Onillon, M. Anisotropy of electrical properties in α-Fe_2O_3 ceramics. *J. Mater. Sci.* **1993**, *28*, 6029−6034.
(48) Boudjemaa, A.; Boumaza, S.; Trari, M.; Bouarab, R.; Bouguelia, A. Physical and photo-electrochemical characterizations of α-Fe_2O_3. Application for hydrogen production. *Int. J. Hydrogen Energy* **2009**, *34*, 4268−4274.
(49) Polyakov, A. O.; Kiseleva, T. Y.; Novakova, A. A.; Grigoryeva, T. F.; Barinova, A. P. Step-by-step powder composite mechanosynthesis for functional nanoceramics. *J. Phys.: Conf. Ser.* **2010**, *217*, 012081.
(50) Xiang, Y.; Yang, Z.; Wang, S.; Hossain, M. S. A.; Yu, J.; Kumar, N. A.; Yamauchi, Y. Pseudocapacitive behavior of the Fe_2O_3 anode and its contribution to high reversible capacity in lithium ion batteries. *Nanoscale* **2018**, *10*, 18010−18018.

https://doi.org/10.1021/acsomega.1c00640
ACS Omega 2021, 6, 12615−12622